On the Growth Regimes of Hydrogen Bubbles at Microelectrodes

Bashkatov, A.; Hossain, S. S.; Mutschke, G.; Yang, X.; Rox, H.; Weidinger, I. M.; Eckert, K.;

Perma-Link to Publication Repository of HZDR:

https://www.hzdr.de/publications/Publ-35502

Journal Name

On the Growth Regimes of Hydrogen Bubbles at Microelectrodes[†]

Aleksandr Bashkatov[*abc], Syed Sahil Hossain[a], Gerd Mutschke[a], Xuegeng Yang[a], Hannes Rox[a], Inez M. Weidinger [d] and Kerstin Eckert[*abc]

The growth of single hydrogen bubbles at micro-electrodes is studied in an acidic electrolyte over a wide range of concentrations and cathodic potentials. New bubble growth regimes have been identified which differ in terms of whether the bubble evolution proceeds in the presence of a monotonic or oscillatory variation in the electric current and a carpet of microbubbles underneath the bubble. Key features such as the growth law of the bubble radius, the dynamics of the microbubble carpet, the onset time of the oscillations and the oscillation frequencies have been characterized as a function of the concentration and electric potential. Furthermore, the system's response to jumps in the cathodic potential has been studied. Based on the analysis of the forces involved and their scaling with the concentration, potential and electric current, a sound hypothesis is formulated regarding the mechanisms underlying the micro-bubble carpet and oscillations.

Broader context

For a successful transition towards a net-zero-emissions industry, it is crucial to replace fossil fuels such as natural gas by renewable energy sources. One promising technology is water electrolysis using solar- or wind-derived electricity to produce high-purity hydrogen gas. However, the costs of water electrolysis today are still higher compared to conventional methods such as steam methane reforming. A crucial constraint when using this technique is the mass transport of the gaseous reaction products hydrogen and oxygen within the electrolyzer. One approach to both reduce the costs and improve the overall efficiency is to enhance the bubble detachment from the electrode. The evolving gas bubbles occupy the electrode surface and thus reduce the rate of the electrochemical reaction. This makes it highly desirable to develop electrodes with improved bubble detachment.

If the bubble dynamics is better understood, the design and the operational parameters of water electrolyzers can be further optimized to elevate the bubble departure and transport in the device. This work provides a detailed overview of the different bubble growth regimes over a broad range of operational parameters. The relevant forces governing the bubble dynamics are summarized, and their scaling with respect to the experimental parameters is analyzed. In addition, the causes of the described phenomena are discussed and partially complemented with simulation results to gain a better understanding of the forces involved.

1 Introduction

Water electrolysis is likely to become a central technology in the carbon-neutral energy system of the future, as it allows electrical energy from renewable sources to be transformed into chemical energy[1]. The hydrogen produced can be used directly as a fuel or serve as a feedstock for further conventional chemicals such as ammonia and hydrocarbons[2–5]. However, the large-scale production of hydrogen requires the process to become more efficient. In conventional alkaline and Proton Exchange Membrane (PEM) electrolyzers, considerable losses are caused by the generated hydrogen and oxygen bubbles, which increase the activation overpotential at the electrodes by blocking electrocatalytic sites and also raise the Ohmic cell resistance[6–9].

As the dynamics of the electrogenerated bubbles are known to have quite a complex local influence on various variables involved in the electrolysis process, e.g. the concentration overpotential[10], supersaturation[7,11] and number of nucleation sites[12], a better understanding of all aspects of the hydrogen bubble evolution is desirable. The knowledge gained will help develop new strategies for rapidly and efficiently removing bubbles from catalytic sites. This, of course, could equally be beneficial for other catalytic re-

[a] Institute of Fluid Dynamics, Helmholtz-Zentrum Dresden-Rossendorf, Bautzner Landstrasse 400, Dresden, 01328 Germany; E-mail: a.bashkatov@hzdr.de
[b] Institute of Process Engineering and Environmental Technology, Technische Universität Dresden, Dresden, 01062 Germany; E-mail: k.eckert@hzdr.de
[c] Hydrogen Lab, School of Engineering, Technische Universität Dresden, Dresden, 01062 Germany
[d] Fakultät Chemie und Lebensmittelchemie, Technische Universität Dresden, Zellescher Weg 19, 01069 Dresden, Germany

actions, including gas formation[13].

In the following, we focus on an investigation of the gas evolution at micro-electrodes. Apart from making the experimental observation of the bubble evolution easier, as a small nucleation area can be examined[14], micro-electrodes can also be considered a generic model for studying the local bubble evolution at catalytic sites of porous or mesh-like electrodes[15–17]. Numerous studies have been performed in the past to better understand how bubble evolution proceeds via nucleation, growth, and detachment[6,14,17–24]. Aspects of the nucleation of H_2 nanobubbles, such as the activation energy, the critical nuclei size or the nanobubble stability, have been addressed by White et al.[25–27] In the subsequent growth phase, the radius R of the bubble versus time t can be described by a power law

$$R(t) = \beta t^x$$

with β and x denoting the growth coefficient and the power exponent[19]. The short initial stage of the growth phase, lasting only for $\mathcal{O}(ms)$, is governed by liquid inertia and characterized by $x = 1$[19,28,29]. Depending on whether the diffusion of hydrogen dissolved in the bulk electrolyte[19,28–31] or direct injection of the gas at the bubble foot, via coalescence with smaller hydrogen bubbles[14,20,21,32,33] is the dominating growth mechanism, the classical exponents $x = 1/2$[31] or $x = 1/3$[33] are observed. The detachment, governed by the balance of forces[34,35] (see Section 3), results from either bubble unpinning processes, such as the neck of the electrode-attached bubble breaking[6], or from a loss of contact with the carpet of microbubbles underneath[36]. In the case of acidic electrolytes, both the lifetime and the detachment diameter of the H_2 bubbles increase along with the cathodic potential or current density[19,21,36–43]. Meanwhile, the situation with alkaline electrolytes is more heterogeneous, with opposite trends sometimes being observed by different groups[44–48]. In fact, the coalescence behavior of bubbles is strongly influenced by the pH value and ion-specific effects of the electrolyte studied[49]. Hydrogen bubbles are known to coalesce more easily in acidic H_2SO_4 than in alkaline KOH solutions[50,51].

Hydrogen bubbles evolve subject to competition between buoyancy, which stimulates the bubbles to rise from the electrode, and the forces attracting them to the electrode, e.g. see Hossain et al.[35] and Section 3. Despite early speculation on the origin of the bubble return phenomenon[28], the Marangoni[35,40,52–54] and electric forces[35,36] have only recently been studied intensively and were both found to retard the bubble departure at micro-electrodes. An initial theoretical consideration of the thermocapillary effect on electrogenerated bubbles in general was provided by Guelcher et al.[55], later supplemented by reasoning on possible solutocapillary effects by Lubetkin et al.[56]. Initial measurements of the circulating Marangoni flow pattern around electrogenerated hydrogen bubbles were carried out by Yang et al.[40]. Later, Massing et al.[52] were able to show that this flow is mainly driven by the thermocapillary effect at the micro-electrode. Hossain et al.[53] extended the simulation study on the thermocapillary effect to include electrodes of different sizes. Later, numerical work by Meulenbroek et al.[54] provided arguments explaining the remaining quantitative differences in the flow profiles observed in the experiment and computation[52] by including surfactant effects at the bubble interface. Apart from capillary effects causing forces on the bubble, there is evidence that the electrostatic bubble-electrode interaction proposed in Coehn et al.[57] and Brandon et al.[19] may also exert a force on the electrogenerated bubbles. In strongly acidic electrolytes, in which the pH is below the iso-electric point, the hydrogen bubbles acquire a positive surface charge due to proton adsorption[58–60]. Thus, they experience an attracting electric force towards the cathode. Only recently, hydrogen bubble dynamics have been shown to transition from conventional stationary to oscillatory growth prior to departure[35,36]. By carefully analyzing the bubble dynamics, a quantitative value for the surface charge density of the hydrogen bubbles was derived. Based on this, it was possible to explain the position oscillations of the bubble based on the non-linear variation in the electric force with the bubble position.

Furthermore, a higher optical resolution allowed a better observation of the thin carpet of microbubbles covering the micro-electrode, above which the "main" hydrogen bubble evolves in an acidic electrolyte[14,36]. The bubble growth is driven by continuous and rapid $\mathcal{O}(\mu s)$ coalescence between the main bubble and the microbubbles of the carpet, following only approximately the growth law with the exponent $x = 1/3$[14]. The question of whether these coalescence events make a significant contribution to the balance of forces affecting the electrogenerated bubble has not yet been resolved. Zhou et al.[61] claimed that the interaction between a boiling bubble and smaller bubbles located beneath it retards detachment. Similarly, reversals in the motion of electrogenerated bubbles recently found under microgravity were shown to be caused by coalescence with bubbles of moderate size, especially at higher cathodic potentials[42].

The present work extends previous studies[14,35,36] by providing a systematic view of the complex phenomena of the electrolytic bubble evolution at a micro-electrode. By characterizing important variables such as the carpet thickness, the onset of bubble oscillations or the bubble elongation over a wide range of cathodic potentials and electrolyte concentrations, distinct growth regimes can be deciphered. A regime map is provided which unifies the three bubble growth regimes observed.

2 Experimental Method

Hydrogen bubbles were produced by water electrolysis in H_2SO_4 of 0.1...1 mol L^{-1} under potentiostatic conditions of -2...-10 V. The electrolyte was prepared using sulfuric acid with a concentration of 1 mol L^{-1} (Carl Roth GmbH + Co. KG). This was diluted to lower concentrations by adding ultrapure water (PURELAB Chorus, 18.2 MΩ.cm). The electrochemical cell sketched in Figure 1a is a cuboid glass cuvette with dimensions of $10 \times 10 \times 40$ mm^3. A $\varnothing 100$ μm Pt micro-electrode is embedded in the glass base. The three-electrode system is completed by two $\varnothing 0.5$ mm Pt wires inserted vertically from the top to serve as the anode and the pseudo reference electrode. The cathode potentials are measured with respect to the pseudo reference electrode (Pt wire, $\approx$ 0.48 V vs. reversible hydrogen electrode RHE for 0.5 M), with the exception of the results provided in Fig. 10, where the potential is
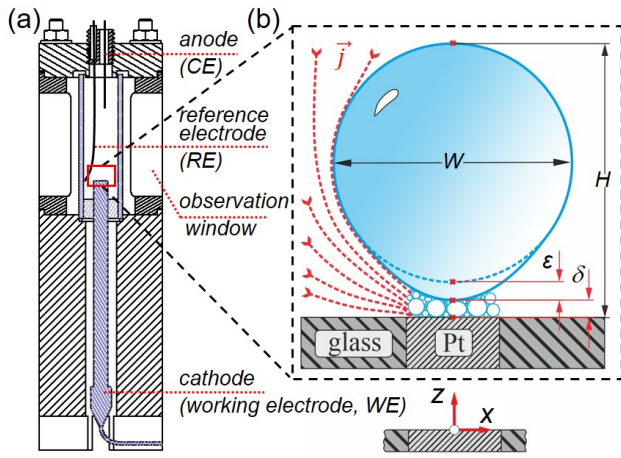
Fig. 1 (a) Electrochemical cell consisting of three electrodes, embedded in protective housing. Reprinted from Bashkatov et al.[42]. (b) schematic of the slightly deformed hydrogen bubble sitting on the carpet of microbubbles sandwiched between the bubble and the micro-electrode. Reprinted from Bashkatov et al.[36].

applied versus a mercury-mercurous sulfate electrode (MSE, 0.65 V vs. SHE). The electrochemical cell is connected to an electrochemical workstation (Zahner Zennium). For each experimental run, the electric current was recorded with a sampling rate of 1 kHz over the 30 s, unless noted differently. The surface of the cathode was polished and thoroughly rinsed with pure water before the measurement campaign. To minimize the scatter, most of the measurements were made with the same cathode on the same day (except the results presented in Section 4.5 and ESI-3[†]).

The cell features two observation windows for simultaneous imaging of the bubble evolution over time. For that purpose, a shadowgraphy system was used. It combines Köhler illumination with a microscope (Thalheim SpezialOptik Pulsnitz, Germany, spatial resolution of 1000 pix/mm), connected to a high-speed IDT camera (Os7 - S3). The recording was carried out at 1000 frames/s, if not mentioned otherwise.

The combination of a micro-electrode and sulfuric acid makes it possible to produce single hydrogen bubbles that periodically detach and are a very similar size[14,40]. Figure 1b presents a schematic of the slightly deformed spherical H_2 bubble, sitting on the working electrode (Pt), and the carpet of microbubbles beneath, together with the lines of the electric current density $\overrightarrow{j}$ directed from the anode to the cathode. All relevant geometric parameters studied in this work are indicated: H — bubble height, W — bubble width, ε — bubble elongation reflecting its deformation and δ — thickness of the carpet. The geometric parameters H, W and δ were extracted by image processing carried out on the shadowgraphs based on the Canny edge detection method described in Matlab R2019b (see the Supplemental Material in Bashkatov et al.[36]). The elongation of the bubble foot is calculated as $\varepsilon = H - W - \delta$.

At low cathodic potentials and spherical bubbles, the bubble radius is $R = W/2$. For non-spherical bubbles, the radius R of the bubble is presented as the equivalent radius of a sphere, the volume of which was obtained from the the current measured

using Faraday's law[14], unless noted otherwise.

The hydrogen bubble evolution was studied for 30 s for each value of concentration and potential. To eliminate the possible influence of small fluctuations in the bubble evolution, the results are averaged over the number of H_2 bubbles formed in 30 s, typically approx. 8 bubbles. As fewer [more] than 8 bubble cycles occur at a high [low] cathodic potential, the respective type of averaging will be clearly stated.

3 Theoretical: Forces on H_2 bubbles

The correct interpretation of the dynamics of the hydrogen bubble at the micro-electrode (Fig. 1) requires an understanding of the governing forces. Essentially, four forces matter: buoyancy, the hydrodynamic force[35,54], the electric force[36] and the interaction force between the gas carpet and the bubble. Buoyancy, which is the only force acting upwards and is thus responsible for bubble detachment, is given as

$$\overrightarrow{F_b} = \frac{4}{3}\pi R^3 \Delta\rho \overrightarrow{g}, \tag{1}$$

where $\Delta\rho$ is the density difference between the gas and the liquid, and g is the gravitational acceleration. The electric force, $\overrightarrow{F_e}$, originates in the action of the electric field that exists in the electrolyte with respect to the electric charge adsorbed at the bubble interface. It is quantified by

$$\overrightarrow{F_e} = \int_{\mathscr{S}} \sigma_s \overrightarrow{E} \, dA. \tag{2}$$

σ_s is the surface charge density of the bubble interface and $\overrightarrow{E}$ is the electric field vector. $\mathscr{S}$ denotes the bubble interface. As a first approximation, we assume that the proton adsorption at the gas-liquid interface, which is the surface-charge-dominating species below the iso-electric point (pH 2...3)[19], is governed by Henry's law. Hence, the surface charge density σ_s is proportional to the concentration c.
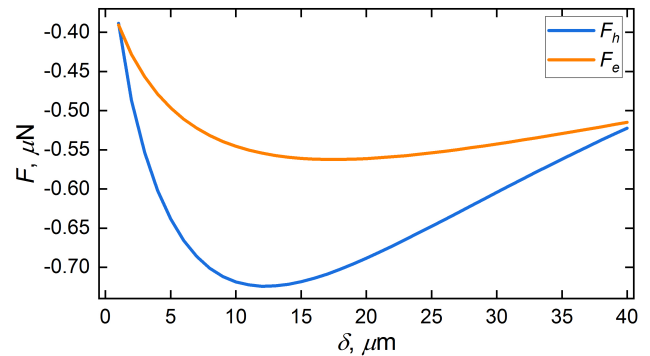

Fig. 2 Variation in hydrodynamic force (F_h) and electric force (F_e) with carpet thickness (δ). The parameters used in the simulations are: $R = 304\,\mu m$, $\phi_c = -3$ V, $\Theta = 80$, $\kappa_{el} = 12$ S/m, $\sigma_s = 1.32$ mC/m^2.

The hydrodynamic force, $\overrightarrow{F}_h$, originates in the electrolyte flow in the vicinity of the hydrogen bubble, and is given as

$$\overrightarrow{F}_h = \int_{\mathscr{S}} \overrightarrow{\tau_h} \, dA. \tag{3}$$

Here, $\vec{\tau_h} = -p_h\vec{n} + \mu\frac{\partial\vec{u}}{\partial n} + \mu\nabla u_n$ is the hydrodynamic boundary stress. p_h is the hydrodynamic pressure, μ is the dynamic viscosity of the electrolyte, $\vec{u}$ is the electrolyte velocity vector, $\vec{n}$ is the surface-normal unit vector, and $u_n = \vec{u}\cdot\vec{n}$.

It has been shown that the electrolyte flow at the bubble interface is primarily driven by thermocapillarity[40,52–54] that originates in a significant temperature gradient along the bubble interface. The temperature gradient was found to be largely caused by the highly concentrated Joule heating, given by $|\vec{j}|^2/\kappa_{el}$, at the foot of the bubble. $\vec{j}$ is the local current density vector in the electrolyte and κ_{el} is the electric conductivity of the electrolyte. The generated heat is then advected along the interface by the Marangoni flow. Diffusion of heat is of minor importance only. A characteristic Peclet number describing the ratio between convective and diffusive heat transfer can be estimated as follows. When assuming an interface velocity U of 10 mm/s[52] at a bubble of radius $R = 300$ μm, $Pe = U\cdot R/\alpha = 180$ where α denotes the thermal diffusivity of the electrolyte. Typical Marangoni numbers for a temperature difference of about 10 K amount to $Ma = \beta_V\cdot\Delta T\cdot R/(\mu\cdot\alpha) = 10^4$ and underline the importance of the thermocapillary effect. Here, β_V denotes the volumetric thermal expansion coefficient, and μ denotes the dynamic viscosity of the electrolyte[52]. As $\vec{j} = \kappa_{el}\vec{E}$, both F_h and F_e are strongly influenced by the current density/electric field that exists in the electrolyte.

To investigate the dependence of F_e and F_h on the carpet thickness δ, parametric simulations of $F_e(\delta)$ and $F_h(\delta)$ are carried out in COMSOL 5.5. The parameters and methodology of the simulation are given in the caption and the ESI-1[†], respectively. Fig. 2 shows that F_e and F_h exhibit similar behavior. Both forces act downward and increase in strength as δ increases. At certain values of δ, F_e and F_h reach their respective maximum values and decrease with a further increment in δ. This change in the electric force can be understood as being caused by a change in the electric field due to variations in the carpet thickness[36], cf. Equation 2. The hydrodynamic force variation arises from a change in current density with varying carpet thickness, which both modifies Joule heating and the location of the temperature maximum at the bubble surface, which in turn changes the flow structure and thus the force, cf. Equation 3.

Finally, the interaction force between the carpet and bubble, $\vec{F}_{g-g}$, includes the effect of bubble coalescence. These events, even for bubbles of different sizes, are responsible for a shift in the center of mass toward the electrode. Such reversals of the bubble movement following coalescence were shown recently in a microgravity environment[42]. However, a quantitative expression for $\vec{F}_{g-g}$ does not yet exist, to the best knowledge of the authors. In the absence of the micro-bubble carpet, the contact pressure force[34] and the surface tension force also need to be considered. The surface tension force, given by

$$F_s = -2\pi r_c\gamma\sin\theta, \tag{4}$$

acts at the three-phase contact line due to surface tension. γ is the surface tension, θ is the contact angle and r_c is the contact radius. The contact pressure force, given by

$$F_{cp} = \frac{2\gamma}{R}\pi r_c^2 \tag{5}$$

can be thought of as the excess Laplace pressure acting on the contact area and is directed upward.

As F_s and F_{cp} do not exist in the dominant case of bubbles growing on a micro-bubble carpet (Fig. 1b), the balance of forces in the vertical direction is given by

$$F_b + F_h + F_e = 0, \tag{6}$$

neglecting the unknown F_{g-g}. If buoyancy F_b wins the competition with F_e and F_h, the bubble detaches.

4 Results

Figure 3 provides an overview of the phenomena observed during a systematic increase in the cathodic potential. The starting point is the temporal behavior of the current during the evolution cycle of single bubbles, shown in Fig. 3a. The time axes are normalized with the respective bubble lifetime, T, at the cathode. Each cycle starts with the nucleation of the bubble and terminates with its detachment. The bubble growth in between leads to an increasing blockage of the active electrode area, which forces the electric current to enter a plateau.

This behavior of the electric current is that of the classical bubble growth studied in previous works[14,21,33,35,36,38,40–42,52,62–65] and found at low cathodic potentials. This behavior is referred to as *Regime I*, see Fig. 3b. It is characterized by the growth of nearly spherical bubbles on top of a carpet of micro-bubbles (see red circle), and monotonic variations in both the position of the apex of the bubble (at height H) and the electric current. The transient of the bubble radius $R(t)$ in sub-figure b(1) is plotted in two versions, which closely match: via image analysis (dashed line) and via the bubble volume using Faraday's law (solid line). The features of Regime I are described in Section 4.1.

For a cathodic potential $\geq$ -3.8 V, the monotonic variation in the current is abruptly replaced by the electric current oscillating rapidly, as displayed for -4 V in Fig. 3a. This type of electric current transient is referred to as *Regime II*, see Fig. 3c. As elaborated earlier, this oscillating electric current is related to vertical oscillations of the bubble position, expressed as oscillations in the bubble apex, H, see sub-figure c(2). The growth of the bubble again proceeds on top of a carpet of micro-bubbles, see enlarged image in c(3). The thickness of the carpet of microbubbles covering the micro-electrode varies periodically[36]. Regime II is further detailed in Sections 4.1 and 4.2.

When the cathodic potential is increased further, these oscillations disappear again, as first observed at -7 V in Fig. 3a. A third *Regime III* starts, which is characterized by bubble growth without a carpet underneath. In Regime III, the largest bubbles are produced; these experience noticeable shape deformations prior to their departure. The remaining oscillations in the current response prior to departure are caused by instabilities in the shape of the bubble neck at the micro-electrode, as will be discussed in Section 4.3.
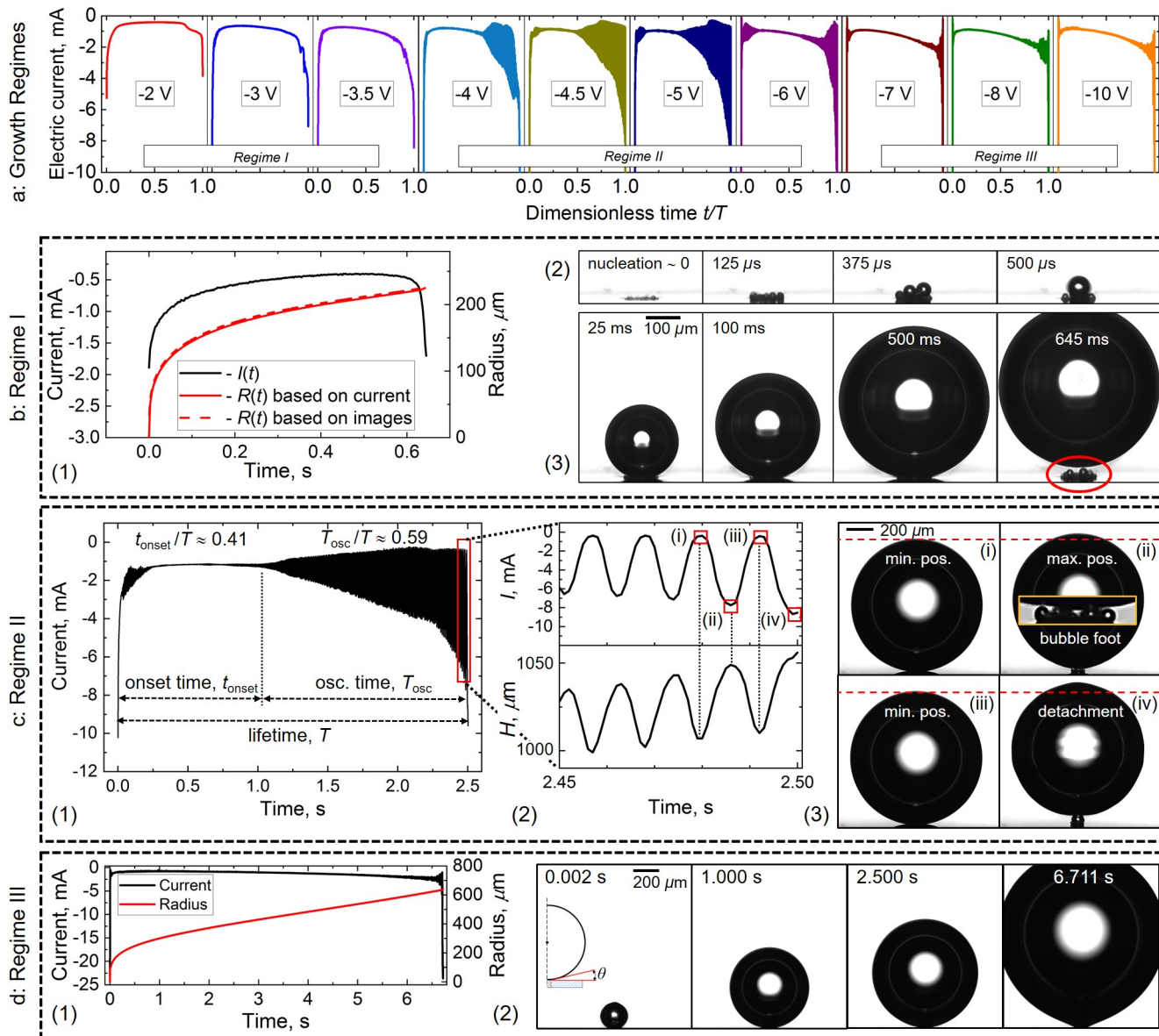
Fig. 3 a) Change in the electric current versus time t, normalized with the bubble lifetime T, upon increasing the cathodic potential ($c = 1$ mol L^{-1}). b)-d) Representative transients of the electric current and bubble images for the three different bubble regimes marked at the bottom of subfigure a) (see main text). b)-d) represents the bubble evolution in 0.5 mol L^{-1} at -2 V, in 0.5 mol L^{-1} at -7 V and in 1 mol L^{-1} at -10 V, respectively. The potential is given vs. pseudo RE (Pt wire).
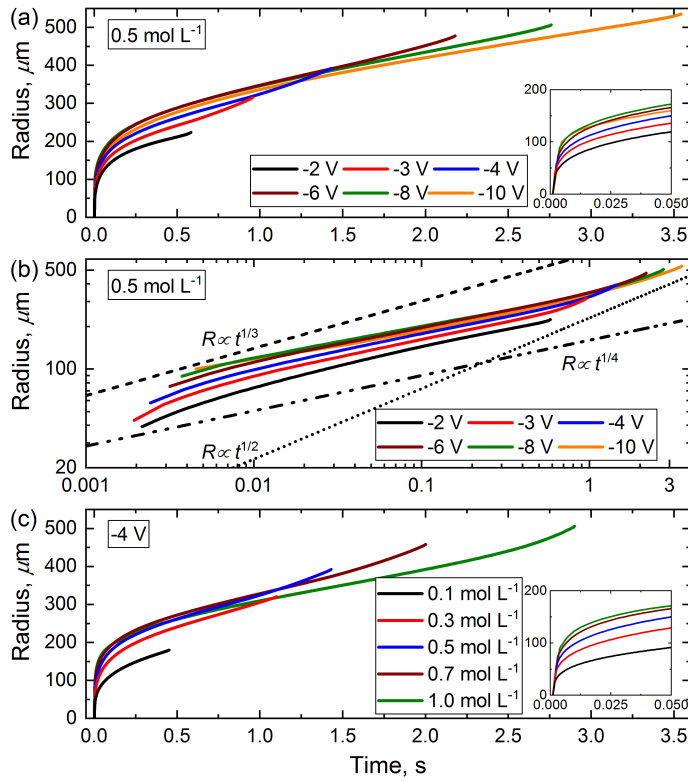
Fig. 4 (a) $R(t)$ for different potentials and an electrolyte concentration of 0.5 mol L^{-1}. (b) $R(t)$ from (a), reproduced in double logarithmic scale. (c) $R(t)$ for different electrolyte concentrations at a fixed potential of -4 V. Each line starts from nucleation and ends at the detachment, and is the result of averaging over 8 bubbles. The insets show the initial phase of the bubble evolution. The potential is given vs. pseudo RE (Pt wire).

In the initial phase of the bubble cycle, further small-scale oscillations are found. In this case, these are the strongest at -6 V. They are caused by bubble position oscillations in the lateral direction, i.e. from the left to the right-hand side (and vice versa), and are beyond the scope of the present study.

The temporal evolution of the bubble radius, driven by the transient electric current within the evolution cycles, is shown in Figure 4a for different cathodic potentials at a fixed electrolyte concentration of 0.5 mol L^{-1} and (c) for various electrolyte concentrations at a fixed potential of -4 V. The radius data $R(t)$ shown were averaged over 8 bubble cycles. Each line starts from nucleation and ends at the detachment. The insets represent the initial first 50 ms of the bubble evolution, and are characterized by a clear trend: the higher the cathodic potential or the higher the concentration, the faster the bubble grows. However, this trend weakens and saturates at high concentration values. Similarly, at the high cathodic potential of -10 V, the speed of growth even becomes smaller than at -8 V. Fig. 4b represents the data from subfigure (a) in a double logarithmic plot to draw conclusions on the exponent x of $R \propto t^x$ during bubble growth. The black dashed and dotted lines added represent the theoretical growth modes of $x = 1/3$ and $x = 1/2$. Additionally, a dashed-dotted line for the case of $x = 1/4$ is inserted. As can be seen, the slopes of the

growth curves and thus the exponents of the growth law change over time. Initially, the behavior is close to $x = 1/2$, but after several milliseconds the exponent quickly decreases to $x = 1/3$ and even converges to $x \approx 1/4$, the faster the potential rises. Then, the exponent remains nearly constant for a relatively long time. This is, in particular, true for the high cathodic potentials (i.e. -8 V and -10 V). When the grown bubble is close to departure, the exponent rises again; it reaches $x \approx 1/3$ at lift-off. This variation in the bubble growth exponent over time is related to the potentiostatic mode applied in the experiments and also to the specifics of the evolution of large bubbles at the micro-electrode.

As shown in Fig. 3, the electric current, which determines the bubble growth rate, depends on the bubble size. Moreover, the carpet thickness and the growth regime exert an influence, as will be discussed below. A similar situation involving time-varying growth exponents is found at different electrolyte concentrations, as shown in Fig. 4c. Here, the power coefficient at 1 mol L^{-1} is also close to, or even slightly below 1/4 (not shown).
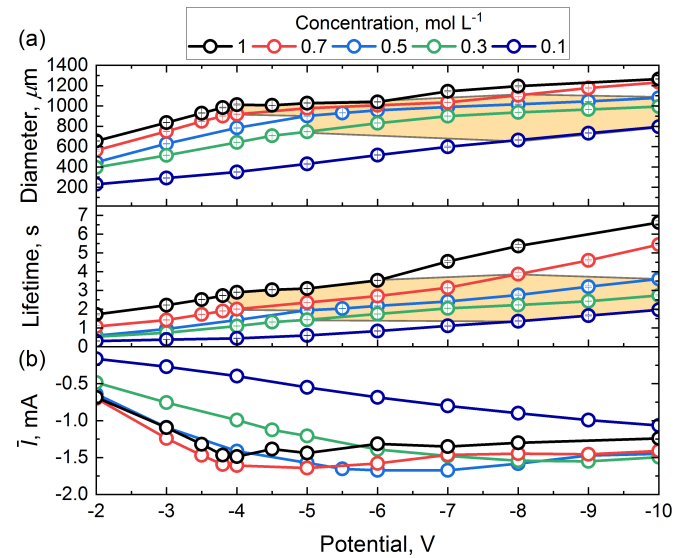

Fig. 5 (a) Detachment diameter $\overline{d}$, bubble lifetime $\overline{T}$ and (b) mean electric current $\overline{I}$ versus the cathodic potential applied at different electrolyte concentrations. The shaded region marks the oscillatory bubble Regime II. All data shown are averaged over the respective number of complete bubble cycles within a period of 30 s. The electrical current is the mean value, additionally averaged over the bubble cycles. The standard deviations of $\overline{d}$ and $\overline{T}$ are mostly below 1% and given as error bars. The latter are not useful for $\overline{I}$ due to the current oscillations in Regime II. The potential is given vs. pseudo RE (Pt wire) if not mentioned otherwise.

The evolution of the bubble radius versus time, can be used to determine the detachment radius of the bubble and its lifetime. The lifetime of the bubble at the electrode is terminated when the balance of forces is violated (see Eq. 6). As the buoyancy force scales $\sim R^3$, the lifetime measures how fast the bubble reaches the critical diameter of departure. Fig. 5a shows that the detachment diameter $d = 2R$ and the bubble lifetime T increase with increasing cathodic potential and increasing concentration. The parameter region of Regime II, shaded in orange, shows the plateau-like behavior of the detachment diameter when the cathodic potential increases. This plateau is especially well resolved at the higher

concentrations (1, 0.7 and 0.5 mol L^{-1}).

Fig. 5b shows the mean electric current $\bar{I}$ averaged over the bubble cycles. The behavior of $\bar{I}$ at the micro-electrode, and thus the mean hydrogen production rate, are mainly affected by the bubble dynamics, which influence the Ohmic resistance. As can be seen, the electric current generally tends to increase with the potential and concentration. However, at concentrations higher than 0.5 mol L^{-1} and potentials larger than -4 V, the trend weakens and even reverses, as clearly seen when comparing the cases of 0.7 mol L^{-1} (red curve) and 1 mol L^{-1} (black curve). For each concentration, a limiting potential exists above which $\bar{I}$ stops increasing and starts to drop again. This limiting potential is smaller at higher concentrations. The phenomenon seems to be related to the plateau-like behavior discussed in subfigure (a) and also the discussion on the initial growth dynamics of the bubbles in Fig. 4. It may be caused by depletion effects suffered by the electrolyte at high mass transfer rates, geometric effects of larger bubbles hindering mass transfer, or modifications to the bubble carpet underneath, which will be discussed below.

4.1 Micro-bubble carpet dynamics and transition from monotonic (Regime I) to oscillatory (Regime II) currents

The basic features of Regime I are summarized in Figure 3b for the evolution of the first bubble at -2 V in 0.5 mol L^{-1}. As soon as the potential is applied ($t = 0$), a strong current is observed, see sub-figure b(1). Bubble nucleation immediately starts at the electrode. Sub-figure b(2), at a frame rate of 8000 s^{-1}, shows numerous micro-bubbles forming the so-called bubble carpet. Rapid coalescence events takes place within two frames, i.e. in less than 125 μs, with continuously generated small bubbles making up the carpet. After approx. 500 μs a single, or *mother* bubble is formed with a typical size of about $R \approx 30\ \mu$m. Fig. 3b(3) shows the further growth of the bubble which is responsible for the reduction of the current in b(1). When the bubble detaches from the electrode, here at $t = 645$ ms, the carpet remains, and the electric current reaches a maximum again.

Next, the dynamics of the *micro-bubble carpet* during the bubble evolution are investigated. Figure 6a shows a magnified image of the foot of the bubble, where the micro-bubble carpet is located (Regime I: 0.3 mol L^{-1} and -4 V). The thickness of the carpet, $\delta(t)$, is seen to increase during bubble growth and reach a maximum at departure, here at $t = 1.049\ s$.

Fig. 6b resolves the temporal dynamics of the carpet thickness, compared with the bubble radius over the bubble lifetime in Fig. 6c, for different cathodic potentials (0.3 mol L^{-1}). All data are obtained from image analysis where the spatial resolution of the optical system is about 1 μm. The inset in (b) defines three characteristic times: the first appearance of the carpet at t_1, the start of the oscillations at t_{onset}, and finally the instant shortly before detachment t_{crit}. As already anticipated in Fig. 6a, δ increases with the growth of the bubble radius. However, this increase proceeds in two different modes: monotonic growth (unfilled symbols) and oscillatory growth (solid line). For the lower cathodic potentials, -3 V and -4 V at 0.3 mol L^{-1}, the monotonic growth of the carpet is the exclusive mode. This holds true for the entire Regime I.
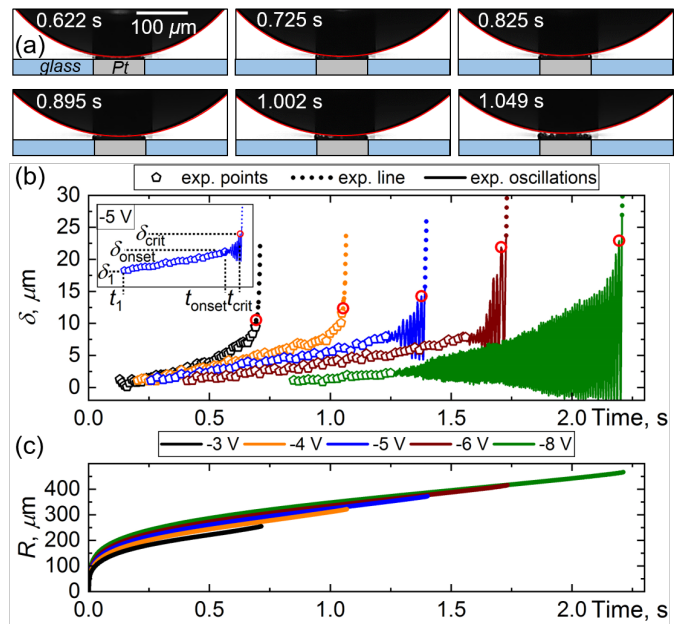

Fig. 6 (a) Magnified images of the evolution of the carpet in Regime I. For support, the circular bubble shape is marked in red. Concentration 0.3 mol L^{-1}, potential at -4 V. (b) Temporal evolution of the carpet thickness δ and (c) the bubble radius at different potentials (vs. pseudo RE (Pt wire).); concentration 0.3 mol L^{-1}. The oscillatory behavior in δ is in Regime II.

This behavior changes with higher cathodic potentials (-5, -6 and -8 V), at which a transition from monotonic to oscillatory growth occurs at t_{onset}. These oscillations are the direct fingerprint of the transition from Regime I to Regime II. Indeed, the onset of oscillations in the electric current also leads to a corresponding oscillation in the vertical bubble position (Regime II, cf. Section 4.2), which enables synchronous carpet oscillations. At larger cathodic potentials, the appearance of a carpet of measurable thickness δ_1 is delayed. Furthermore, the carpet thickness, δ_{onset}, is smaller at the onset of the oscillations.

The growth of the carpet lasts until bubble detachment, at which point the critical carpet thickness δ_{crit}, marked by red circles in Fig. 6b, is achieved. The values of δ_{crit} were obtained by averaging over 20 ms (equal to 20 images) before detachment in the case of a monotonic carpet evolution. In the case of oscillatory growth, the value of the penultimate peak before detachment was used. The dotted lines in subfigure (b) show the carpet evolution after detachment.

Figure 7 summarizes the behavior of the critical carpet thickness $\bar{\delta}_{crit}$ versus potential for different concentrations. The data shown were obtained from averaging over 5...8 bubbles, and the error bars are the corresponding standard deviations. For guidance, 3rd-degree polynomial fit curves are added, from which the main trend can be derived. When the cathodic potential is increased to more negative values, at almost all concentrations the critical carpet thickness first increases to reach a peak value of $\bar{\delta}_{crit}^m$, then decreases again. In more detail, as the concentration increases, the peak value of $\bar{\delta}_{crit}^m$ becomes smaller and is shifted towards lower cathodic potentials. At the lowest concentration
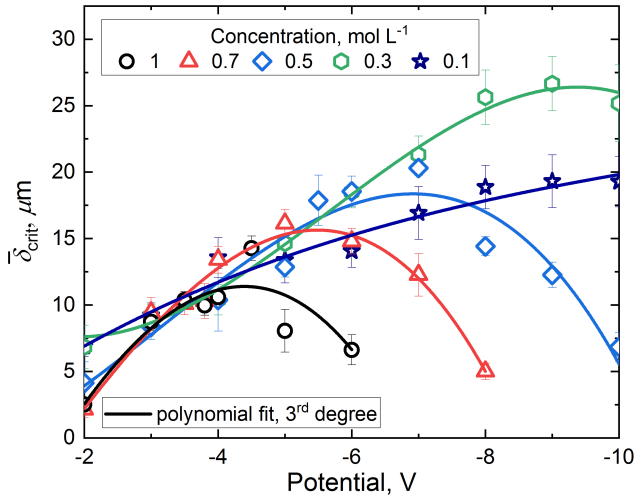
Fig. 7 Critical carpet thickness versus potential (vs. pseudo RE) at different concentrations. The data points result from averaging over 5...8 bubbles. For guidance, 3rd-degree polynomial fit curves are added.

value of 0.1 mol L^{-1}, the peak value may be located outside the studied potential range. Table 1 summarizes the peak values of $\overline{\delta}_{crit}^{m}$ and the respective electrode potentials ϕ_{m1} for the different concentrations c. We note that the ϕ_{m1} values obtained from Fig. 7 coincide with the onset of a plateau-like behavior of $\overline{I}$ in Fig. 5

	Concentration, mol L^{-1}				
	1	0.7	0.5	0.3	0.1
$\overline{\delta}_{crit}^{m}$, μm	14.3	16.1	20.3	26.7	—
ϕ_{m1}, V	-4.5	-5	-7	-9	—

Table 1 Peak values of $\overline{\delta}_{crit}^{m}$ (cf. Fig. 7) and respective potential values ϕ_{m1} for various electrolyte concentrations.

The carpet thickness at detachment, $\overline{\delta}_{crit}$ (Fig. 7), can be considered as the maximum quasi-equilibrium position of the bubble permitted by the given values of ϕ and c. It notably scales with ϕ and c: for a given c, $\overline{\delta}_{crit}$ increases as the potential ϕ becomes larger until a maximum value $\overline{\delta}_{crit}^{m}$ is reached at ϕ_{m1}. This increase is probably caused by the higher current $\overline{I}$, leading to a higher bubble nucleation rate. For $\phi > \phi_{m1}$ the trend reverses, and the carpet thickness $\overline{\delta}_{crit}$ decreases again. This decrease in the carpet height is also reflected in Fig. 6b.

4.2 Regime II: Oscillatory bubble growth

Figure 3c(1) shows the evolution of the current in Regime II for the example of -7 V and 0.5 mol L^{-1}. We see that a transition from monotonic toward oscillatory growth occurs at $t_{onset}/T = 0.41$, i.e. after 41% of the lifetime T of the bubble at the electrode. A magnified image of the final current oscillations prior to departure is shown in Fig. 3c(2) together with the transient of the bubble apex, height H as introduced in Fig. 1. The last four instants when the current reaches a maximum or minimum value during the oscillation are marked by red squares and are labeled (i) to (iv). Fig. 3c(3) shows the bubble images at these instants in time, with the dashed red line additionally marking the position of H at the time of the first minimum (i). It is obvious that the

local maxima of H and I are in phase, i.e. the cathodic current reaches a maximum at the highest bubble position. The inset in (ii) shows the micro-bubble carpet at the moment the bubble is at the highest position of the last oscillation phase. The carpet thickness oscillates together with the bubble position as already shown in Fig. 6b. When the bubble reaches a maximum height H, the space between the bubble foot and the electrode surface is also at a maximum, which allows the micro-bubble carpet to expand and the current to grow, as the electrode is less blocked by the bubble. When the bubble moves toward the electrode to attain the minimum H, the thickness of the bubble carpet decreases until it is no longer visible (iii). During the oscillations, the amplitudes of the current, top position H and carpet thickness δ rise until critical values are reached at which the bubble detaches.

The frequency of the oscillations is calculated from $f = 1/\Delta t$, with Δt denoting the time interval between two consecutive maxima (or minima). The frequency and amplitude of the electric current oscillations are detailed in ESI-2† (Figure S1) and summarized in Figure 8 for different concentrations. Figure 8 plots the non-dimensional onset time $\overline{t}_{onset}/\overline{T}$ in (a), the dimensionless radius $\overline{R^*}$ (b) and the frequency of the current oscillations versus the potential applied (c). Here, $\overline{R^*} = \overline{R}_{onset}/\overline{R}$ is the ratio between the radii at the onset and detachment, respectively. All data show the mean and the error margin from averaging over 8 bubbles.
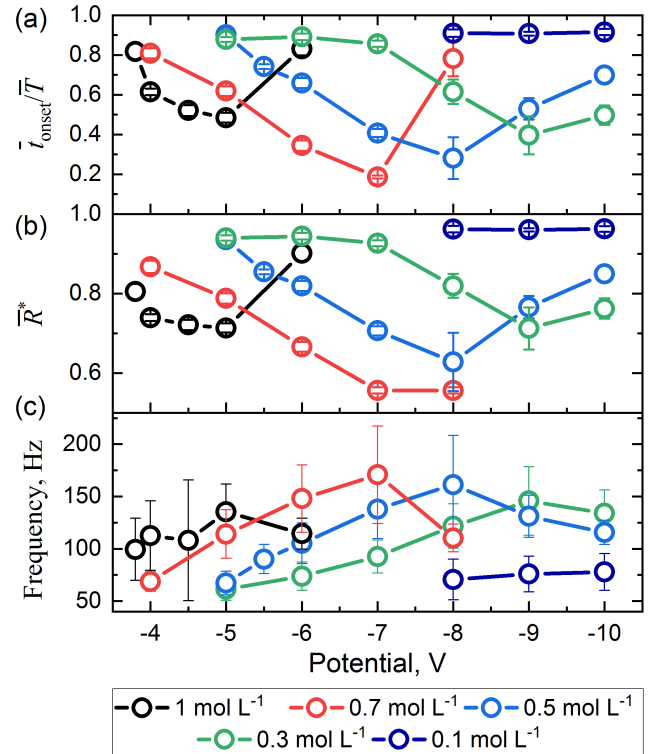
Fig. 8 Characterization of the oscillatory behavior in Regime II: (a) Dimensionless onset time. (b) Dimensionless radius $\overline{R^*}$. (c) Frequency of the electric current. The data show the mean and error margins from averaging over 8 bubbles. For further details see the text. The potential is given vs. pseudo RE (Pt wire).

To explain the main trends seen in Fig. 8 we first focus on the case of $c = 1$ mol L^{-1} (black curves). At a potential of -3.8 V, the

oscillations set in when the bubble has reached roughly 80% of its final radius at approx. 80% of the bubble lifetime. For higher cathodic potentials, the dimensionless onset time decreases, in line with a smaller dimensionless bubble radius at the onset. At a potential of $\phi_{m2} = -5$ V, all three variables attain local extrema (black curve, 1 mol L^{-1}). Thus, at -5 V the oscillations start at the earliest time (at given $c = 1$ mol L^{-1}), hence with the smallest possible bubble radius. The small bubble size means the frequency can reach its highest level ($\overline{f} \sim 140$ Hz) as less electrolyte mass needs to be accelerated in line with the spring model of oscillations[36]. Afterwards, the trend is reversed, and the onset time and $\overline{R}^*$ increase again with increasing cathodic potential. This pattern is found for all concentrations > 0.1 mol L^{-1}. Impressively, the duration of the oscillations can take up to 80% of the bubble lifetime (0.7 mol L^{-1}, -7 V) starting at a radius $\overline{R}_{onset}$ of about 0.556 $\overline{R}$, equivalent to a bubble volume of $\overline{V}_{onset} = 0.172 \overline{V}$.

4.3 Regime III: Monotonic growth of non-spherical bubbles without micro-bubble carpet

The features of the bubble evolution in Regime III are presented in Figure 3d at -10 V and 1 mol L^{-1}. The electric current again varies monotonically as in Regime I, see d(1). A single bubble with a radius $R = 89$ μm is formed by coalescence after just 2 ms, see Fig. 3d(2). The rest of the bubble evolution proceeds smoothly, without any measurable micro-bubble carpet, hence seemingly without coalescence, and therefore presumably by diffusion, until the detachment at a size of $R = 641$ μm. Minor perturbations in the current are visible shortly before detachment caused by instabilities in the bubble neck, which repeatedly disconnects from and reconnects with the electrode. Since there is no micro-bubble carpet, it is possible to measure the contact angle between the adhered bubble and the electrode surface. As shown in Fig. 9a, the contact angle drops rapidly after nucleation to reach a broad minimum during growth, before again rising to about 28 degrees at departure.

Bubble growth in Regime III is characterized, besides the absence of the carpet, by a stretching of the bottom part of the bubble. We quantify this in terms of elongation ε (cf. Fig. 1(b)). The critical elongation of the bubble before detachment, $\overline{\varepsilon}_{crit}$, is plotted in Figure 9(b) vs. potential for different electrolyte concentrations, averaged over 5...8 bubbles. The error bars are the corresponding standard deviations. The elongation $\overline{\varepsilon}_{crit}$ increases with both the cathodic potential and concentrations. The highest value of $\overline{\varepsilon}_{crit} \sim 80 \mu$m is measured at 1 mol L^{-1} at -10 V, which is equal to 13% of the detachment radius. Note that a certain elongation of the bubble is present in all three regimes. However, it is considerably smaller in Regimes I and II, where a carpet exists.

Finally, we note here that Regime III stays at high concentrations when even higher cathodic potentials are applied than those studied so far. The behavior that is found comes to be dominated by vertical *shape oscillations* of the strongly deformed bubble, which are clearly different from the *position oscillations* of the bubble in the case of Regime II. In Figure 10, three consecutive bubble images are shown in 1 mol L^{-1} at -12 V (vs MSE — a mercury-mercurous sulfate electrode, 0.65 V vs SHE) to visualize
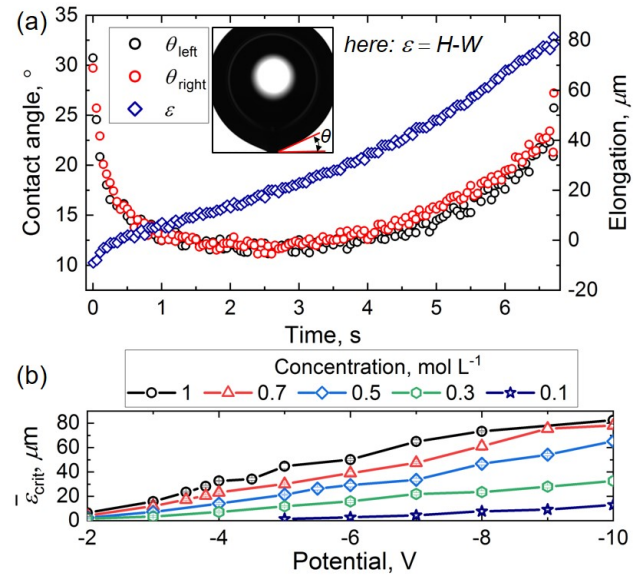

Fig. 9 (a) Variation in contact angle and elongation over time during one bubble cycle in Regime III (1 mol L^{-1} at -10 V). (b) Critical elongation $\overline{\varepsilon}_{crit}$ before the bubble detaches vs. potential at various concentrations. Each point represents a value averaged over 5...8 bubbles. The potential is vs. pseudo RE (Pt wire).

the oscillations in the shape. During these oscillations, the bubble remains attached to the electrode. The high potentials of -12 V in 1 mol L^{-1} are beyond the operating limit of the electrode as the high current densities might damage the micro-electrode. Therefore, it is difficult to obtain results with robust statistics.
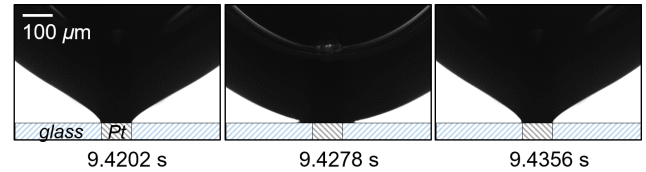

Fig. 10 Beyond Regime III (1 mol L^{-1} at -12 V): Vertical oscillations in shape at high potential. The snapshots show the bubble in its upper, lower and again upper position shortly before detachment. Time counts from nucleation. The lifetime in this particular case is $T = 9.4360$ s. Image recording at 5380 frames/s. The potential is vs. MSE.

4.4 Regime map

The three bubble growth regimes described so far occur in different regions of the parameter space spanned by ϕ and c. Their location is summarized in the regime map shown in Fig. 11. Here, the experiments (and their repetitions) performed for a specific combination of (ϕ, c) are indicated by regime-specific symbols (e.g. squares for Regime I). Each symbol or experiment hides the $I(t)$ and $R(t)$ transients which were shown by way of example in Figs. 3 and 4. Hence, the regime map in Fig. 11 is actually a three-dimensional plot, simplified to a 2D plot for greater clarity. Red circles correspond to experiments on the boundary between two regimes. Polynomial fits mark these boundaries by dashed lines.
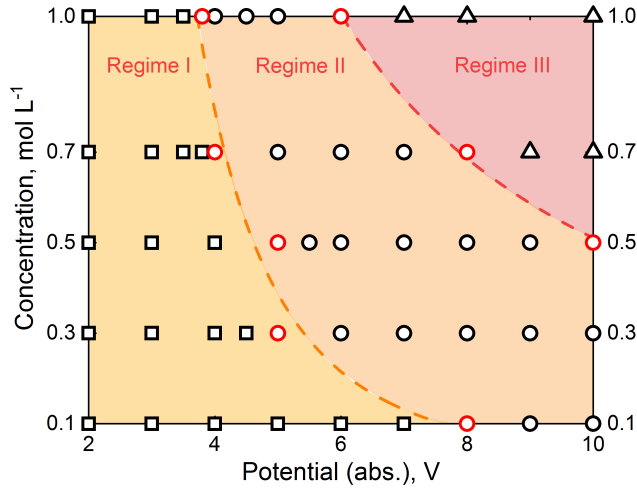
Fig. 11 Regime map showing the three different regimes of bubble growth as a function of cathodic potential (vs. pseudo RE) and electrolyte concentration. Red circles indicate experiments at the border between different regimes. The regime borders (dashed lines) are fitted by $c = a \times |\phi|^b$.

In Table 2 we collect insightful data taken from the experiments marked with red circles at the boundary between Regime I and Regime II (orange dashed line) exactly at the onset time $t_{onset}(c, \phi)$ of oscillatory growth.

c, mol L^{-1}	ϕ, V	$\bar{\delta}$, μm	$\bar{W}$, μm	$\bar{\varepsilon}$, μm	$\bar{I}$, mA
1	-3.8	2.93	811	16.3	1.51
0.7	-4	3.23	803	15.6	2.12
0.5	-5	5.79	851	17.7	2.48
0.3	-5	6.40	712	9.40	1.49
0.1	-8	11.8	648	6.80	1.06

Table 2 Data depicted at $t_{onset}(c, \phi)$ along the border between Regimes I and II in Fig. 11. Bubble width $\bar{W}$, carpet thickness $\bar{\delta}$, elongation $\bar{\varepsilon}$ and $\bar{I}$ were averaged over 8 bubbles.

Table 2 shows that a reduction of the concentration shifts the transition from Regime I to II at higher cathodic potentials ϕ (2nd column) accompanied by an increase in the carpet thickness $\bar{\delta}$ (3rd column). The size of the bubble (width $\bar{W}$) at t_{onset} first slightly increases to reach a maximum at the intermediate concentration $c = 0.5$ mol L^{-1}, then decreases again. The same trend is observed for the bubble elongation $\bar{\varepsilon}$ and the current $\bar{I}$.

For further illustration of the different bubble regimes, videos are available in ESI†.

4.5 Bubble response to jumps in potential

To check the robustness of the regimes identified, the system's response to jumps in the potential was analyzed. First, the carpet response to a sudden rise in the cathodic potential $\phi_1 = -5$ V, applied for 0.7 s, to $\phi_2 =$ -6, -7, -8 and -10 V is studied in Figure 12. As the bubble evolution at fixed ϕ_1 proceeds with nearly identical $I(t)$ and $R(t)$ transients (Fig. 12a), the bubble size in the four experiments is identical before jumping from ϕ_1 to ϕ_2. At the moment the potential is swapped, a peak in the current appears, the

magnitude of which is proportional to ϕ_2. Afterward, the current relaxes quickly. The increase in the radius is consistently slightly steeper for -10 V compared to -6 V (see inset). The curves stop at $t = 1.2$ s due to bubble detachment caused by the potential interruption ($\phi_3 = 0$ V).

Most importantly, simultaneously with the jump in the potential, the bubble moves closer to the electrode. This can be seen from the images of the foot of the bubble before and after the jump $\phi_1 \rightarrow \phi_2 = -8$ V in Fig. 12b. This movement happens quickly, within several ms. The thicknesses of the carpet at ϕ_1, $\bar{\delta}_{\phi_1}$, and at ϕ_2, $\bar{\delta}_{\phi_2}$ are summarized in Table 3.
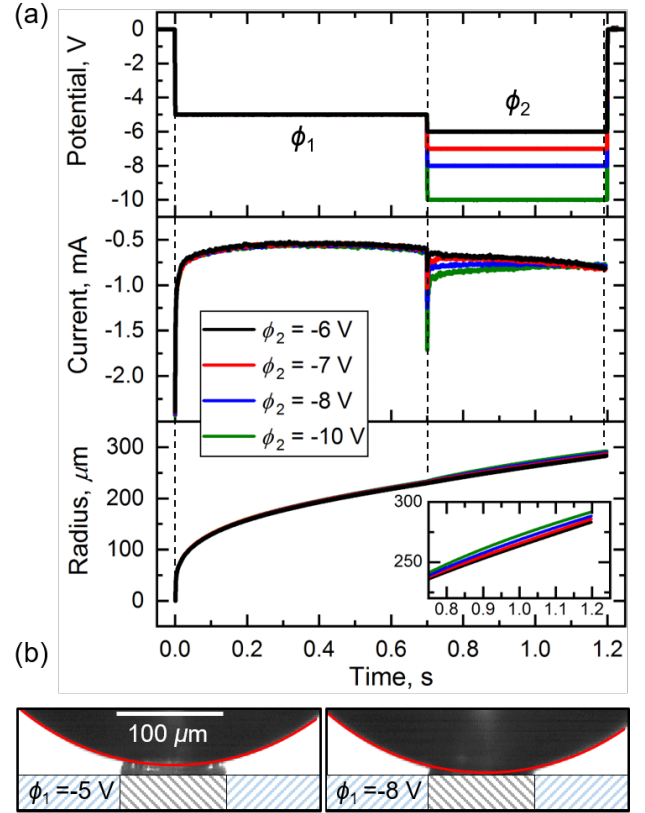

Fig. 12 Response to jumps in the potential in Regimes I and II: (a) Applied jumps from $\phi_1 = -5$ V $\rightarrow \phi_2 \rightarrow \phi_3 = 0$ V at 0.1 mol L^{-1} and resulting $I(t)$ and $R(t)$ transients. (b) Images of the micro-bubble carpet before and shortly after the jump from -5 V to -8 V (vs. pseudo RE).

ϕ_2, V	$\bar{\delta}_{\phi_1}$, μm	SD, μm	$\bar{\delta}_{\phi_2}$, μm	SD, μm	$\Delta_{\bar{\delta}_{\phi_1} - \bar{\delta}_{\phi_2}}$, μm
-6	6.2	0.5	3.6	0.4	2.6
-7	6.4	0.6	2.7	0.4	3.7
-8	6.6	0.4	1.3	0.6	5.3
-10	7.2	0.5	≈ 0	≈ 0	7.2

Table 3 Thickness of the carpet before ($\bar{\delta}_{\phi_1}$) and after ($\bar{\delta}_{\phi_2}$) the jump in the potential from ϕ_1 to ϕ_2 for various ϕ_2. Each value was averaged over 20 ms (20 images) before and after the jump in potential for every individual bubble and over 5 bubbles. SD is the standard deviation. $\Delta_{\bar{\delta}_{\phi_1} - \bar{\delta}_{\phi_2}}$ represents the reduction in the carpet thickness caused by the jump in the potential.

The reduction in the carpet thickness from $\bar{\delta}_{\phi_1}$ to $\bar{\delta}_{\phi_2}$, expressed by $\Delta_{\bar{\delta}_{\phi_1} - \bar{\delta}_{\phi_2}}$, increases along with ϕ_2 until no resolvable

carpet is left: this happens at -10 V at the given bubble radius.

The response to the jumps in the cathodic potential of both developed oscillations in the current and the transition from Regime III → II is presented in ESI-3† (Figure S2). These experiments underline the fact that the oscillations are a very robust phenomenon and that an instantaneous transition from Regime III to Regime II can be achieved by suddenly lowering the cathodic potential. For further illustration of the behavior at the jumps of the potential, videos are available in ESI†.

5 Discussion

By applying high electric potentials ϕ considerably exceeding that in industrial electrolyzers, we were able to analyze the evolution of hydrogen bubbles under extreme conditions and for a wide range of electrolyte concentrations, c. The new bubble growth regimes detected shed more light on bubble dynamics in general, and especially the underlying balance of forces, cf. Section 3 and Hossain et al.[35].

The basic features of bubble growth as a function of c and ϕ can be understood to a zeroth approximation using a simplified version of Ohm's law without the concentration part: $I = \phi/R_{el}$. The ohmic resistance is given by $R_{el} = l/(\kappa_{el}A)$. It depends on the electrode area A, on the current path length l, changes in which are neglected, and on electrical conductivity κ_{el}, which is controlled by the concentration of the electrolyte. In differential form, the increment of the current, dI, is given by

$$dI = \frac{\kappa_{el}}{l}(A\,d\phi + \phi\,dA). \tag{7}$$

dI increases with increasing values of κ_{el} (hence c), and ϕ. dI decreases with growing bubble size as the electrode becomes deactivated, i.e. $dA < 0$, if the bubble size exceeds that of the micro-electrode.

In the initial phase of bubble growth after nucleation, the speed of growth is strongly determined by the values of ϕ and c (Fig. 4 and Fig. 6). At an intermediate stage, when the bubble is already large compared to the size of the micro-electrode, the growth rate is much less dependent on potential and concentration, and largely determined by the geometry, implying an elevated ohmic resistance (cf. Eq. 7). As the bubble carpet grows over time in Regimes I and II (see Fig. 6b), the ohmic resistance decreases slightly, and the bubble growth rate again becomes moderately dependent on the potential and concentration.

The features of all three regimes, including the diameter at which the bubble detaches, are governed by the forces acting on the bubbles. To better understand the interplay between buoyancy (F_b), which is responsible for bubble detachment, and the attracting forces, electric force, F_e, hydrodynamic force, F_h and the bubble-carpet interaction F_{g-g}, we next analyze their scaling with the radius, potential and concentration. When the charge density is assumed to be constant, F_e scales with the surface size of the bubble $\sim R^2$ and the applied potential ϕ. As the surface charge density is known to further depend on the pH, the bulk concentration is also important, so apart from saturation effects at high concentrations $F_e \sim c \cdot \phi \cdot R^2$.

The hydrodynamic force originating from the thermocapillary effect is slightly more complex. As the bubbles grow close to the electrode wall, the main force components result from the balance of the thermocapillary stress (F_M) and the pressure (F_p), with the latter dominating[35,54]. From Lubetkin et al.[66] and Zeng et al.[67] it is known that $F_M \sim \frac{\partial\gamma}{\partial s}R^2$. The gradient of the surface tension is caused by the Ohmic dissipation $\sim I^2$ and reduced by the advection of heat due to the interfacial flow. As known from earlier work, the interfacial velocity scales as $u \sim I$ (see Yang et al.[40]). We therefore assume that $F_M \sim I \cdot R^2$ applies approximately. On the other hand, the thermocapillary flow reduces the pressure at the bubble foot, and the resulting pressure force is $F_p \sim \Delta p \cdot R^2$. Assuming that $\Delta p \sim u$ due to extreme viscous friction near the wall, and again using $u \sim I$ from Yang et al.[40] we finally arrive at $F_p \sim I \cdot R^2$. This agrees with the scaling derived for F_M, which is not surprising, as F_p originates in F_M. For the following scaling analysis, we assume that the pressure component of the hydrodynamic force F_p dominates compared to the Marangoni part F_M.

The poorly understood bubble-carpet interaction, F_{g-g}, is expected to increase along with the number of small bubbles in the carpet; thus it should scale $\propto I$. Table 4 again summarizes the scaling of all forces with ϕ, c and R as well as their characteristic values. Additionally, contact pressure and surface tension forces, which are only relevant in Regime III, are included. We also draw

Forces	Formulation	Scaling	Direction
F_b	Eq. 1	$\sim R^3$	↑
F_e	Eq. 2	$\sim c\phi R^2$	↓
F_h	Eq. 3	$\sim IR^2$	↓
F_s	Eq. 4	$\sim \gamma r_c \sin\theta$	↓
F_{cp}	Eq. 5	$\sim \frac{\gamma r_c^2}{R}$	↑

Table 4 Forces acting on the bubble and their scaling with operating parameters and bubble radius. An upward arrow implies that the force acts in $+z$ direction for the coordinate system defined in Figure 1b and the downward arrow indicates the opposite. The scaling of F_{g-g} is left for future studies.

attention to the fact that for a bubble in Regime III growing on a solid surface (Fig. 9(a) at $t = 5$ s), the downward-directed surface tension force (-5.74 μN) is considerably smaller than the upward-directed forces, the contact pressure force (2.02 μN) and the buoyancy force (6.36 μN), detailed in ESI-4†. Thus, with respect to the balance of forces, an immediate bubble departure would be expected, but this is not observed. This lends credence to the existence of other downward-acting forces i.e. the electric force and the hydrodynamic force, as already discussed in the present contribution and elsewhere in the literature[35,36,52–54]. In this context, we would also like to point out that the Fritz equation[6,13,68], derived based on the balance of forces (buoyancy and surface tension) for a bubble attached to a solid surface, is not expected to apply in the presence of a micro-bubble carpet (Regimes I and II). Additional effects from contact line pinning might further influence the departure dynamics[54] in Regime III.

Table 4, together with the spatial dependence of F_e and F_h on δ (Fig. 2), helps gain a qualitative understanding of the most

striking results, namely the existence and the features of the bubble carpet (Regime I and II) and the bubble oscillations (Regime II). We start by discussing the *bubble carpet*. The formation of the carpet is obviously coupled to two constraints: (i) non-equal rates of bubble nucleation (faster) and bubble-bubble coalescence (slower), and (ii) not to high attractive forces, i.e. moderate potentials and concentrations. As H_2SO_4 is an electrolyte that does not inhibit coalescence [49,69], issue (i) is fulfilled. The microbubbles in the carpet have a typical lifetime of $\mathcal{O}(\mu s)$, and the carpet thickness δ increases linearly over time at a given c and ϕ, see Fig. 6b. This growth of the carpet relates to the fact that the buoyancy force which scales like R^3 cannot be fully compensated for by the weaker growing hydrodynamic and electric forces, which scale with R^2. As a result, the quasi-equilibrium position of the growing bubble, which is equivalent to the carpet thickness, increases with time.

ϕ, V	δ, μm	I, mA	W, μm	ε, μm	F_e, μN	F_h, μN
-4	6.43	1.21	607	5.97	-0.48	-0.53
-5	3.86	1.09	608	6.23		
-6	2.66	1.13	608	6.33	-0.55	-0.61
-8	0...1	1.24	611	5.50		

Table 5 Impact of ϕ on the carpet thickness δ at comparable bubble widths and elongations ε. Data depicted from Fig. 6 at a fixed bubble radius of 305 μm; concentration 0.3 mol L^{-1}. For spherical bubbles, $R = W/2$, otherwise R is calculated as an equivalent radius. For two cases, the electric and the hydrodynamic force, F_e and F_h, values as obtained from simulations are listed (carpet coverage $\Theta = 99$, surface charge density $\sigma_s = 1.32$ mC/m^2). For details of the simulations, see Hossain et al. [35].

Table 5 shows data of the carpet thickness δ extracted from Fig. 6b at different potentials ϕ but at a fixed bubble radius R of 305 μm. With higher cathodic potentials ϕ, the carpet thickness δ reduces; it reaches the resolution limit at -8 V. Most notably, the current remains approximately constant. This implies that according to Eq. (7) the reduction in the surface area (-dA), associated with the reduction in δ, is approximately compensated for by the higher cathodic potentials. For two potentials, the numerical values of the hydrodynamic force F_h and also the electric force F_e as obtained from simulations are added in Table 5. Both, F_e and F_h grow larger at higher cathodic potentials. Thus, the simple scaling laws derived in Table 4 need to be extended to include the strong influence of the carpet thickness on the electric and the hydrodynamic force, as documented in Fig. 2. Taking into consideration that a carpet of microbubbles does not appear at comparable conditions in microgravity [42], it is quite likely that the carpet thickness is mainly adjusted by the balance of F_b, F_e and F_h, and F_{g-g} plays only a minor role.

This is also supported by the concentration dependence of $\overline{\delta}_{crit}^m$ shown in Fig. 7. When c increases, both the value of $\overline{\delta}_{crit}^m$ and ϕ_{m1} decrease, i.e., the maximum occurs even with a smaller cathodic potential (ϕ). Characteristic data in Fig. 7, summarized in Table 6, are: $\overline{\delta}_{crit}^m \sim 14.3\,\mu$m at $\phi_{m1} \sim -4.5$ V for $c = 1$ mol L^{-1}, and $\overline{\delta}_{crit}^m \sim 26.7\,\mu$m at $\phi_{m1} \sim -9$ V for $c = 0.3$ mol L^{-1}. Notably, ϕ_{m1} correlates rather well with the maximum of the average current $\bar{I}$ (Fig. 5b and Table 6). Hence, the system adjusts $\overline{\delta}_{crit}^m(\phi_{m1}, c)$ such that the current is nearly identical. Thus, at the lower concentration or conductivity, a thicker carpet is needed for the same current to occur. Therefore, we can again conclude that the Marangoni forces are the same for the 26.7 μm carpet at 0.3 mol L^{-1} and the 14.3 μm at 1 mol L^{-1}.

Two further observations support the role played by F_e in regulating the carpet thickness. Fig. 12 and Table 3 show that a sudden jump in ϕ to larger negative values instantaneously compresses the carpet to a smaller δ. Finally, in Regime III, at high cathodic potentials ϕ or high F_e, there is no carpet at all.

As a second important result of this work, three different bubble growth regimes have been identified and characterized in detail. The appearance of a specific growth mode depends on the potential and concentration and was summarized in a regime map (Fig. 11). The most striking phenomenon is the transitions from Regime I to Regime II, in which the current oscillates.

The experiments offer evidence that the bubble position oscillations in Regime II are coupled to the existence of the carpet. First, there are no position oscillations in the carpet-free Regime III, but they can be instantaneously initiated from Regime III by a jump in the potential into the range where the carpet forms (for details see ESI-3†, Fig. S2b). Second, the oscillations require a certain minimum carpet thickness (Fig. 6b). Thus, one can hypothesize that the carpet is the source of the perturbation when the bubble is at a transient equilibrium position, triggering the onset of the oscillations in the bubble position. Obviously, a sufficiently high cathodic potential is the precondition to create the required level of perturbation, as the oscillations do not occur at a lower ϕ in Regime I. The perturbations most likely consist in *locally* higher bubble nucleation and/or coalescence rates. As a result, the bubble is probably kicked out of its transient equilibrium position at the symmetry line of the electrode. Buoyancy wins for a short time and the bubble rises a short distance. The resulting increase in carpet thickness δ leads to an increase in the electric force F_e until a maximum is reached, see Fig. 2. Second, as the larger δ allows a higher current to flow, the Marangoni convection is intensified, which leads to a further reduction in the pressure. Thus F_h increases and also pulls the bubble towards the electrode. Third, the coalescence rate might also be increased if the bubble is attracted to the electrode due to F_e and F_h.

Three feedback mechanisms seem to be at work, keeping the oscillations running: (i) With decreasing δ, F_e becomes weaker again [36], and the current decreases. As a result, (ii) the Marangoni force simultaneously diminishes. (iii) By contrast, the buoyancy increases, pulling in the opposite direction, as the bubble further grows by coalescence. Thus, another oscillation cycle may start.

The dependence of $\bar{t}_{onset}/\bar{T}$ and $\bar{R}^*$ on the concentration, depicted in Fig. 8, shows a similar but mirror-symmetric behavior to $\overline{\delta}_{crit}$ in Fig. 7. They decrease with increasing ϕ until minimum values are reached at ϕ_{m2}. Thus, with growing ϕ the oscillations set in earlier and hence at a smaller dimensionless bubble radius. For $|\phi| > |\phi_{m2}|$ this trend reverses again and the start of the oscillations is shifted to later times and hence larger bubble sizes. At ϕ_{m2}, the corresponding frequency of the bubble oscillations is

c, mol L^{-1}	$\overline{\delta}^{m}_{crit}(\phi_{m1})$, μm	ϕ_{m1}, V	$\overline{I}$, mA	ϕ_{m2}, V	$\overline{R}^{*}_{min}$	$\overline{R}_{detach}$, μm	$\overline{f}(\phi_{m2})$, Hz
1.0	14.3	-4.5	-1.39	-5	0.712	513	135
0.3	26.7	-9	-1.55	-9	0.713	483	146
	Fig. 7	Fig. 7	Fig. 5c	Fig. 8	Fig. 8	Fig. 5a	Fig. 8

Table 6 Quantitative data from Figs. 5, 7 and 8, which show, based on the example of two concentrations, the correlation between the maximum carpet thickness $\overline{\delta}^{m}_{crit}$ at ϕ_{m1} and the minimum in the relative bubble radius $\overline{R}^{*}_{min}$ at which the oscillations set in, which occurs at ϕ_{m2}.

always at a maximum. This is plausible as the volume of the electrolyte which needs to be displaced is small, hence the fluid inertia, as the bubble size is minimal. The averaged frequencies from Fig. 8c may attain maximum values of up to 170 Hz. The disappearance of the oscillations in the current in Regime III further supports the hypothesis that these fast oscillations require the existence of a carpet that is able to quickly adapt its thickness in time.

In the case of sessile gas bubbles beneath a heated wall, it is known from other work that different modes of oscillatory bubble deformation occur as the Marangoni number rises. Here, transverse oscillations are found to occur first, earlier than axial oscillations, which are likely to be suppressed by the bubble-wall contact. Consequently, much lower frequencies are also observed than those found in our case[70,71].

The similarities between Figs. 8 and 7 are addressed in Table 6 for two concentrations: 1 mol L^{-1} (black line) and 0.3 mol L^{-1} (green line). We note first that $\phi_{m2} \approx \phi_{m1}$. Thus, the minima of $\overline{t}_{onset}/\overline{T}$ and $\overline{R}^{*}$ occur at nearly the same potential where $\overline{\delta}^{m}_{crit}$ is attained. Second, the bubble radii at which the earliest onset occurs ($\overline{R}^{*} \approx 0.7$) and the detachment radii (approx. 1000 μm) are nearly the same, hence the oscillation frequencies ($f \sim 140$ Hz). Third, as already mentioned above, the corresponding currents $\overline{I}$ are identical, adjusted by the different carpet sizes δ. Thus the question arises of why the bubble oscillations are nearly identical despite the vastly different values of c and ϕ_{m2} in Table 6. As the ratio between buoyancy and the attracting forces is probably decisive, and buoyancy is nearly the same in both cases, the sum of the attracting forces F_M and F_e needs to be the same. Indeed, the lower concentration (0.3 mol L^{-1}) leading to a lower surface charge is compensated for by a higher ϕ (-9 V) to approach a comparable F_e to (1 mol L^{-1}, -5 V), while F_M is the same on average, as the average current in both cases is similar.

6   Summary and conclusions

The dynamics of H$_2$ bubbles was studied at a Pt micro-electrode in an acidic electrolyte for a broad range of cathodic potentials ϕ and concentrations c. This allowed us to probe the bubble behavior subject to hitherto unexplored ranges of the relevant forces governing bubble detachment (cf. Section 3).

We were able to show that beside the classic monotonic bubble growth, termed Regime I, two further regimes exist (Fig. 11). In the second, Regime II, the apex of the bubble oscillates in phase with the electric current. Regime III is characterized again by monotonic growth, but coupled to major bubble deformations. In all three regimes, the exponent x, describing the increase in the bubble radius over time, $R(t) = \beta t^{x}$, can differ from the classi-

cal ones, $x = 1/3$ ($x = 1/2$) when the bubble growth is controlled by coalescence (diffusion). Exponents even down to $x = 1/4$ are found when the growth rate is determined by the geometry in the case of large bubbles significantly exceeding the electrode diameter. Overall, the bubble detaches later and at a larger size as the cathodic potential and concentration increase.

Furthermore, we were able to resolve the fast micro-scale dynamics of the bubble carpet, which is considered to be the connecting element between Regimes I and II. At each (ϕ, c) combination, the carpet thickness increases during the bubble growth until a value δ_{crit} is reached at detachment (Fig. 6). For a given concentration, $\overline{\delta}_{crit}$ varies in an inverse-parabolic form with the cathodic potential (Fig. 7). This striking behavior, together with the immediate compression of the carpet upon a sudden jump in the potential (Fig. 12), substantiates the hypothesis that the carpet thickness is adjusted by three forces: (i) buoyancy, leading finally to detachment, (ii) the electric force and (iii) the hydrodynamic forces which both attract. The increase in the latter two forces with the cathodic potential causes the carpet to disappear at high potentials, marking the transition to Regime III.

One further important result is the characterization of the remarkable oscillatory growth regime, Regime II. For certain (ϕ, c) combinations (Fig. 11), the monotonic change in the current is replaced at the time t_{onset} by an oscillatory change which occurs in phase with oscillations in the bubble position on top of the microbubble carpet. For each concentration, the onset time of oscillatory growth varies in a now parabolic like manner with the cathodic potential. The earliest onset was found at already 20% of the bubble lifetime, coupled with the highest frequencies (up to 170 Hz).

The improved understanding of the above-mentioned forces in terms of spatial variation (Fig. 2) and scaling (Table 4) makes it possible to hypothesize the origin of the oscillations. The perturbation required to trigger the oscillations is seen in local variations of the bubble nucleation/coalescence rate in the carpet at a sufficiently high cathodic potential. This kicks the bubble out of its quasi-static equilibrium position. Buoyancy forces the bubble to rise. As the electric and hydrodynamic forces both increase with the distance between the bubble and the electrode (Fig. 2), they are able to attract the bubble to the electrode again, giving rise to another oscillation cycle. One unexplored issue is the forces exerted by coalescing bubbles. Here, new methods need to be developed to tackle this highly dynamic processes taking place on small length scales.

As micro-electrodes serve as a model for the electrocatalytic sites in porous electrodes, the present results not only considerably extend our understanding of the forces that determine bub-

ble detachment, but might be informative regarding the further improvement of porous catalysts.

Conflicts of interest

There are no conflicts to declare.

Acknowledgments

List of Symbols

$\vec{a}$	Bubble acceleration, m^2 s^{-1}
$\vec{j}$	Local current density vector, A m^{-2}
$\vec{u}$	Electrolyte flow velocity, m s^{-1}
A	Electrode area, m^2
c	Electrolyte concentration, mol L^{-1}
d	Bubble diameter, m
d_F	Fritz's diameter, m
E	Electric field, N m^{-1}
f	Oscillation frequency, Hz
F_b	Buoyancy force, N
F_e	Electric force, N
F_h	Hydrodynamic force, N
F_i	Forces acting on the bubble, N
F_s	Surface tension force, N
F_{cp}	Contact pressure force, N
F_{g-g}	Carpet-bubble interaction, N
g	Gravitational acceleration, m s^{-2}
H	Bubble height, m
I	Electric current, A
l	Current path length, m
m	Inertia of the motion, kg m^2
m_a	Added mass, kg
m_b	Mass of the bubble, kg
p_h	Hydrodynamic pressure, Pa
R	Bubble radius, m
r_c	Contact radius, m
R_e	Micro-electrode radius, m
R_{el}	Ohmic resistance, kg m^2 s^{-3} A^{-2}
R_{onset}	Bubble radius upon the start of the oscillations i.e. at t_{onset}, m
SD	Standard deviation
T	Lifetime of the bubble, s
t	Time, s
t_1	First appearance of the carpet, s
t_{crit}	Instant of time shortly before detachment, s

t_{onset}	Start of the oscillations, s
T_{osc}	Duration of the oscillations, s
U	Bubble interface velocity, m s^{-1}
V	Bubble volume, m^3
V_{onset}	Bubble volume upon the start of the oscillations i.e. at t_{onset}, m^3
W	Bubble width, m
x	Power exponent of the power law

Greek Symbols

α	Thermal diffusivity of the electrolyte, m^2 s^{-1}
β	Growth coefficient of the power law
β_V	Volumetric thermal expansion coefficient, m^3 K^{-1}
δ	Carpet thickness, m
$\Delta\rho$	Gas-electrolyte density difference, kg m^{-3}
δ_{crit}	Carpet thickness shortly before detachment i.e. at t_{crit}, m
δ_{onset}	Carpet thickness upon the start of the oscillations i.e. at t_{onset}, m
γ	Surface tension, N m^{-1}
κ_{el}	Electric conductivity of the electrolyte, S/m
μ	Electrolyte dynamic viscosity, Pa s
$\vec{\tau_h}$	Hydrodynamic boundary stress, N m^{-2}
ϕ	Cathodic potential with respect to reference electrode, V
ϕ_c	Cell voltage, V
ϕ_{m1}	Cathodic potential providing the local maximum of δ_{crit} in Fig. 7, V
ϕ_{m2}	Cathodic potential providing the local maximum of f in Fig. 8, V
ρ_g	Hydrogen gas density, kg m^{-3}
ρ_l	Electrolyte density, kg m^{-3}
σ_s	Surface charge density, C m^{-2}
Θ	Electrode coverage, 1
θ	Contact angle, °
ε	Bubble elongation, m

Notes and references

1 N. Brandon and Z. Kurban, *Philosophical Transactions of the Royal Society A: Mathematical, Physical and Engineering Sciences*, 2017, **375**, 20160400.

2 L. Barreto, A. Makihira and K. Riahi, *International Journal of Hydrogen Energy*, 2003, **28**, 267–284.

3 F. Mueller-Langer, E. Tzimas, M. Kaltschmitt and S. Peteves, *International Journal of Hydrogen Energy*, 2007, **32**, 3797–3810.

4 N. K. Shah, Z. Li and M. G. Ierapetritou, *Industrial & Engineering Chemistry Research*, 2011, **50**, 1161–1170.

5 W. Lattin and V. P. Utgikar, *International Journal of Hydrogen Energy*, 2007, **32**, 3230–3237.

6 A. Angulo, P. van der Linde, H. Gardeniers, M. Modestino and D. F. Rivas, *Joule*, 2020, **4**, 555–579.

7 X. Zhao, H. Ren and L. Luo, *Langmuir*, 2019, **35**, 5392–5408.

8 J. A. Leistra and P. J. Sides, *Journal of the Electrochemical Society*, 1987, **134**, 2442.

9 J. R. Lake, A. M. Soto and K. K. Varanasi, *Langmuir*, 2022.

10 J. Dukovic and C. W. Tobias, *Journal of the Electrochemical Society*, 1987, **134**, 331.

11 P. Peñas, P. van der Linde, W. Vijselaar, D. van der Meer, D. Lohse, J. Huskens, H. Gardeniers, M. A. Modestino and D. F. Rivas, *Journal of the Electrochemical Society*, 2019, **166**, H769.

12 N. Pande, G. Mul, D. Lohse and B. Mei, *Journal of the Electrochemical Society*, 2019, **166**, E280.

13 P. Lv, H. Le The, J. Eijkel, A. Van den Berg, X. Zhang and D. Lohse, *The Journal of Physical Chemistry C*, 2017, **121**, 20769–20776.

14 X. Yang, F. Karnbach, M. Uhlemann, S. Odenbach and K. Eckert, *Langmuir*, 2015, **31**, 8184–8193.

15 A. Nouri-Khorasani, E. T. Ojong, T. Smolinka and D. P. Wilkinson, *International Journal of Hydrogen Energy*, 2017, **42**, 28665–28680.

16 P. Hadikhani, S. M. H. Hashemi, S. A. Schenk and D. Psaltis, *Sustainable Energy & Fuels*, 2021, **5**, 2419–2432.

17 R. Iwata, L. Zhang, K. L. Wilke, S. Gong, M. He, B. M. Gallant and E. N. Wang, *Joule*, 2021, **5**, 887–900.

18 C. Sillen, E. Barendrecht, L. Janssen and S. Van Stralen, in *Hydrogen as an Energy Vector*, Springer, 1980, pp. 328–348.

19 N. Brandon and G. Kelsall, *Journal of Applied Electrochemistry*, 1985, **15**, 475–484.

20 G. Sakuma, Y. Fukunaka and H. Matsushima, *International Journal of Hydrogen Energy*, 2014, **39**, 7638–7645.

21 D. Fernandez, P. Maurer, M. Martine, J. Coey and M. E. Möbius, *Langmuir*, 2014, **30**, 13065–13074.

22 P. van der Linde, P. Peñas-López, Á. M. Soto, D. van der Meer, D. Lohse, H. Gardeniers and D. F. Rivas, *Energy & Environmental Science*, 2018, **11**, 3452–3462.

23 K. J. Vachaparambil and K. E. Einarsrud, *Applied Mathematical Modelling*, 2021.

24 F. Higuera, *Journal of Fluid Mechanics*, 2021, **927**, A33.

25 L. Luo and H. S. White, *Langmuir*, 2013, **29**, 11169–11175.

26 Q. Chen, L. Luo, H. Faraji, S. W. Feldberg and H. S. White, *The Journal of Physical Chemistry Letters*, 2014, **5**, 3539–3544.

27 S. R. German, M. A. Edwards, H. Ren and H. S. White, *Journal of the American Chemical Society*, 2018, **140**, 4047–4053.

28 D. E. Westerheide and J. Westwater, *AIChE Journal*, 1961, **7**, 357–362.

29 J. Glas and J. Westwater, *International Journal of Heat and Mass Transfer*, 1964, **7**, 1427–1443.

30 P. S. Epstein and M. S. Plesset, *The Journal of Chemical Physics*, 1950, **18**, 1505–1509.

31 L. Scriven, *Chemical Engineering Science*, 1959, **10**, 1–13.

32 H. Verhaart, R. De Jonge and S. Van Stralen, *International Journal of Heat and Mass Transfer*, 1980, **23**, 293–299.

33 R. Darby and M. Haque, *Chemical Engineering Science*, 1973, **28**, 1129–1138.

34 G. Thorncroft and J. F. Klausner, *Multiphase Science and Technology*, 2001, **13**, 35–76.

35 S. S. Hossain, A. Bashkatov, X. Yang, G. Mutschke and K. Eckert, *Physical Review E*, 2022.

36 A. Bashkatov, S. S. Hossain, X. Yang, G. Mutschke and K. Eckert, *Physical Review Letters*, 2019, **123**, 214503.

37 P. J. Sides, in *Modern Aspects of Electrochemistry*, Springer, 1986, pp. 303–354.

38 P. Kristof and M. Pritzker, *Journal of Applied Electrochemistry*, 1997, **27**, 255–265.

39 H. Matsushima, T. Iida and Y. Fukunaka, *Electrochimica Acta*, 2013, **100**, 261–264.

40 X. Yang, D. Baczyzmalski, C. Cierpka, G. Mutschke and K. Eckert, *Physical Chemistry Chemical Physics*, 2018, **20**, 11542–11548.

41 D. Baczyzmalski, F. Karnbach, G. Mutschke, X. Yang, K. Eckert, M. Uhlemann and C. Cierpka, *Physical Review Fluids*, 2017, **2**, 093701.

42 A. Bashkatov, X. Yang, G. Mutschke, B. Fritzsche, S. S. Hossain and K. Eckert, *Physical Chemistry Chemical Physics*, 2021, **23**, 11818–11830.

43 H.-K. Park and B.-J. Chung, *Experimental Thermal and Fluid Science*, 2021, **122**, 110316.

44 H. Vogt and R. Balzer, *Electrochimica Acta*, 2005, **50**, 2073–2079.

45 D. Zhang and K. Zeng, *Industrial & Engineering Chemistry Research*, 2012, **51**, 13825–13832.

46 P. Haug, B. Kreitz, M. Koj and T. Turek, *International Journal of Hydrogen Energy*, 2017, **42**, 15689–15707.

47 J. Venczel, *Electrochimica Acta*, 1970, **15**, 1909–1920.

48 L. Janssen and J. Hoogland, *Electrochimica Acta*, 1973, **18**, 543–550.

49 V. S. Craig, *Current Opinion in Colloid & Interface Science*, 2011, **16**, 597–600.

50 H. Matsushima, T. Nishida, Y. Konishi, Y. Fukunaka, Y. Ito and K. Kuribayashi, *Electrochimica Acta*, 2003, **48**, 4119–4125.

51 H. Matsushima, Y. Fukunaka and K. Kuribayashi, *Electrochimica Acta*, 2006, **51**, 4190–4198.

52 J. Massing, G. Mutschke, D. Baczyzmalski, S. S. Hossain, X. Yang, K. Eckert and C. Cierpka, *Electrochimica Acta*, 2019, **297**, 929–940.

53 S. S. Hossain, G. Mutschke, A. Bashkatov and K. Eckert, *Electrochimica Acta*, 2020, **353**, 136461.

54 A. Meulenbroek, A. Vreman and N. Deen, *Electrochimica Acta*, 2021, **385**, 138298.

55 S. A. Guelcher, Y. E. Solomentsev, P. J. Sides and J. L. Anderson, *Journal of the Electrochemical Society*, 1998, **145**, 1848.

56 S. Lubetkin, *Langmuir*, 2003, **19**, 10774–10778.

57 A. Coehn and H. Neumann, *Zeitschrift für Physik*, 1923, **20**, 54–67.

58 N. Brandon, G. Kelsall, S. Levine and A. Smith, *Journal of Applied Electrochemistry*, 1985, **15**, 485–493.

59 C. Yang, T. Dabros, D. Li, J. Czarnecki and J. H. Masliyah, *Journal of Colloid and Interface Science*, 2001, **243**, 128–135.

60 M. Takahashi, *The Journal of Physical Chemistry B*, 2005, **109**, 21858–21864.

61 J. Zhou, Y. Zhang and J. Wei, *Applied Thermal Engineering*,

2018, **132**, 450–462.

62 Q. Hu, H.-b. Liu, Z. Liu, D. Zhong, J. Han and L.-m. Pan, *Journal of Electroanalytical Chemistry*, 2021, **880**, 114886.

63 D. Baczyzmalski, F. Karnbach, X. Yang, G. Mutschke, M. Uhlemann, K. Eckert and C. Cierpka, *Journal of The Electrochemical Society*, 2016, **163**, E248.

64 H. Liu, L.-m. Pan, H. Huang, Q. Qin, P. Li and J. Wen, *Journal of Electroanalytical Chemistry*, 2015, **754**, 22–29.

65 S. Zhan, Y. Huang, W. Zhang, B. Li, M. Jiang, Z. Wang and J. Wang, *International Journal of Hydrogen Energy*, 2021, **46**, 36640–36651.

66 S. Lubetkin, *Electrochimica Acta*, 2002, **48**, 357–375.

67 B. Zeng, K. L. Chong, Y. Wang, C. Diddens, X. Li, M. Detert, H. J. Zandvliet and D. Lohse, *Proceedings of the National Academy of Sciences*, 2021, **118**, e2103215118.

68 W. Fritz, *Physik. Zeitschr*, 1935, **36**, 379–384.

69 V. Craig, B. Ninham and R. M. Pashley, *Nature*, 1993, **364**, 317–319.

70 C. Chun, D. Raake and G. Hansmann, *Experiments in Fluids*, 1991, **11**, 359–367.

71 M. Kassemi and N. Rashidnia, *Physics of Fluids*, 2000, **12**, 3133–3146.